Nanoscale

ARTICLE

Terahertz phase jumps for ultra-sensitive graphene plasmon sensing

Received 00th January 20xx,
Accepted 00th January 20xx

DOI: 10.1039/x0xx00000x

www.rsc.org/

Yi Huang, [a] Shuncong Zhong,*[a, b] Yao–chun Shen, [a, c] Yingjie Yu, [b] and Daxiang Cui [d]

The phase behavior of the reflected terahertz radiation (THz) under surface plasmon resonance (SPR) supported by doped graphene has been comprehensively investigated. For a TM–polarized wave, the dependence of the phase on the angle of incidence has a region with an abrupt jump–like change. We found in particular that the resonance phase dependence would change from step–like contour to Fano lineshape when the system passed through the optimum SPR conditions (i.e., $R = 0$) in terahertz regime. Monitoring the transformation could provide ultrahigh–sensitive label–free detection of biomolecules. Importantly, the characteristic of phase jumps as a readout response to achieve refractive index sensing that outperforms traditional terahertz–amplitude based attenuated total reflection (ATR) spectroscopy. The results demonstrated a high figure of merit (FOM) of up to 171 based on the terahertz phase information. Moreover, the sensing range could be tuned by changing the surface conductivity of graphene via high doping levels or with few–layer graphene. These terahertz phase response characteristics of graphene plasmon are promising for tunable ultra–sensitivity (bio)chemical sensing applications.

1. Introduction

Terahertz (THz) radiation (0.1 THz–10 THz) has incredibly fascinating prospects for many applications due to their unique properties.[1] As opposed to X–rays, terahertz waves have absolutely non-ionizing radiation impact, are harmlessness for biological entities.[2] More importantly, many complex molecules exhibit unique absorption spectral features result from their vibrational and rotational modes in the THz regime,[3, 4] making THz technology advantages for vast sensing applications in biological and chemical fields.[5, 6] However, the extensive usage of THz spectroscopy in sensing is greatly limited by the detection of small changes of optical property in molecular interactions, due to their too small absorption cross–sections. To overcome the limitation, THz metamaterials use structured metal surfaces with annular holds,[7] periodicity pits,[8, 9] groove array,[10] square brass tubes and brass cylindrical rods[11] have been proposed as platforms for supporting tightly confined fields to enhance light–matter interactions and sharp spectral features to enable the measurement of small changes in the dielectric environment, similar to surface plasmon polariton (SPP) sensing at visible frequency band. Furthermore, the optical properties of SPP modes can be tailored through properly designing their geometric parameters. Nonetheless, these structures have bulky size and complex design, as such cannot be actively tuned. Moreover, their sensing performance need to be further improved.

Recently, experimental and theoretical studies demonstrate that graphene can support plasmons for a wide frequency range from mid–infrared to terahertz with remarkable properties such as high confinement and prominent enhancement of electromagnetic field in the vicinity of graphene surface.[12, 13] Graphene plasmons can propagate for hundreds of microns in the THz regime with effective wavelengths 2–6 times smaller than the excitation wavelength, which can generate strong light–matter interactions.[14] In addition, the plasmonic properties can be dynamically tuned via electrical and chemical doping in real time.[15, 16] These supernormal properties means that graphene could be a very flexible platform on which to conduct dynamically tunable surface plasmons resonance (SPR) for sensing applications.

In the present work, an Otto prism coupling structure with graphene/insulator stack (GIS) was presented to perform refractive index sensing using terahertz phase information. Similar prism coupling structures have been previously used to excite highly confined SPPs wave modes on graphene in THz region.[14] Meanwhile, the traditional method namely angle modulation have been employed to monitor the excitation of surface plasmon (SP) with amplitude measurements within the resonant reflectance dip.[17, 18] However, the ability to properly discern any spectral shifts for small refractive index changes in highly absorbing mediums is very limited because of the low figure of merit ($\mathrm{FOM} = S_n / \mathrm{FWHM}$, where S_n is the sensitivity of SPR system and FWHM is the full width at half maximum of resonant contour. It is calculated to evaluate the performance of refractive index sensing with SPR), which possibly restricting

[a] Laboratory of Optics, Terahertz and Non-Destructive Testing, School of Mechanical Engineering and Automation, Fuzhou University, Fuzhou 350108, P. R. China.
[b] School of Mechatronic Engineering and Automation, Shanghai University, Shanghai 200072, P. R. China.
[c] Department of Electrical Engineering and Electronics, University of Liverpool, L69 3BX, United Kingdom;
[d] Department of Bio-Nano Science and Engineering, Shanghai Jiaotong University, Shanghai 200030, P.R. China

the practical sensing applications. For this reason, we draw attention to an oft–neglected source of information in sensing research that is available via THz–TDS, the phase of the electromagnetic fields. Although Ng, Binghao, et al. experimentally demonstrated that the phase had an abrupt jump–like change near optimum SPR conditions through spoof plasmon surface based Otto prism setup in THz frequency range,[19] complete and comprehensive information on the phase properties of THz–SPR is still lacking. Our aim was to fill this gap and pave the way for novel THz sensing methods using terahertz phase information.

2. Structural design and physical mechanism

Our Otto prism coupling structure based SPR sensing system consisting of GIS was shown in Fig. 1. A thin layer of NFC (which is a derivative of polyhydroxystyrene) with thickness of $t_b = 20$ nm and a refractive index of $n_b = 1.535$ [20] was spin–coated on the top of MgF_2 substrate with a refractive index of $n_s = 1.36$ [21] as a buffer layer to construct a relatively gentle contact for graphene. Experimental studies have shown that the addition of a low dielectric constant polymer buffer layer (NFC) between graphene and dielectrics helps to minimize mobility degradation.[22] A monolayer graphene (MLG) is then transferred onto the top of the buffer layer forming GIS. The SP is excited through the evanescent wave created by total internal reflection at the bottom of prism with a high refractive index of $n_p = 4$.[23] There exists a strong interaction between light and the analyte n_a, when the following condition of momentum matching is satisfied

$$k_{spp} = k_{\parallel} = \frac{2\pi}{\lambda_0} n_p \sin\theta_{in} \tag{1}$$

where k_{spp} is the wavevector of SPP wave, $k_{\parallel}$ is the parallel components of incident THz beam wavevector in the prism k_p, λ_0 is the free-space wavelength and θ_{in} is the internal incident angle. Subsequently, the modulated THz radiation reflects off prism base and exit from the other facet of prism where the modulated THz radiation would be detected. The obtained modulated THz radiation contains two vital important information including: the sharp changes in both amplitude and phase of the THz radiation, which will ensure the measurement of small changes in the dielectric environment.

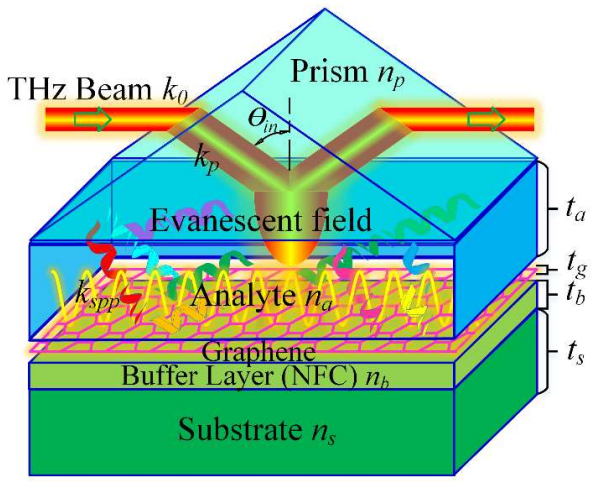

Fig. 1 Schematic diagram of GIS based THz-SPR sensing system via attenuated total reflection (ATR) method.

In the THz regime, the surface conductivity of graphene is dominated by the intraband contribution and can be approximated by a Drude model as: [24]

$$\sigma(\omega) \approx i\frac{e^2 E_F}{\pi\hbar^2(\omega + i\tau^{-1})} \tag{2}$$

where $\hbar$ is the reduced Planck constant, e is the charge of an electron, ω is the incident light angular frequency, E_F is the Fermi level energy of graphene determined by the carrier density $n_0 = (E_F/\hbar v_F)^2/\pi$ (v_F is Fermi velocity), as high as $E_F = 1-2$ eV has been achieved in experiments,[16, 25] and τ is the phenomenological relaxation time which is taken to be 1 ps to account for scattering loss from acoustic phonons.[14, 26, 27] Further, the effective thickness of MLG has been taken to be $t_g = 0.5$ nm[28] with an equivalent dielectric constant as given below:

$$\varepsilon_g = 1 + \frac{i\sigma}{(\omega\varepsilon_0 t_g)} \tag{3}$$

where ε_0 is the permittivity of vacuum; For highly doped MLG, $|\Re\varepsilon_g| \gg |\Im\varepsilon_g|$ in the local limit ($\omega \gg \tau^{-1}$), where $\Re\varepsilon_g$ and $\Im\varepsilon_g$ are the real and imaginary parts of ε_g. This is why graphene can support highly confined SPP modes at THz regime.[14] The contribution of buffer layers to the total conductivity can be ignored due to that buffer layers are thin and non-conducting.[29] Therefore, the total dynamical conductivity is the sum of the conductivities of the individual graphene sheets, *i.e.*, $\sigma_{total} = N\sigma$, where N is the number of graphene layer ($N < 6$).[30] By matching the boundary conditions for the SPR system, the SPP dispersion relation can be derived as:[31]

$$\frac{n_a^2}{k_{za}} + \frac{n_s^2}{k_{zs}} + \frac{iN\sigma}{\omega\varepsilon_0} = 0 \tag{4}$$

If $\Re k_{spp} \gg \Im k_{spp}$ and $k_{spp}^2 \gg k_i^2$, where $k_i = n_i k_0$ ($i = a, s$, $k_0 = 2\pi/\lambda_0$ is wavevector of vacuum), the perpendicular components of the SPP wavenumber $k_{zi} = (k_{spp}^2 - k_i^2)^{1/2} \approx k_{spp}$. Substituting $k_{zi} = k_{spp}$ into Eq. (4) yields the approximation: [27, 31]

$$k_{spp} \approx \frac{\pi\varepsilon_0\hbar^2(n_a^2 + n_s^2)(\omega^2 + i\omega\tau^{-1})}{Ne^2 E_F} \tag{5}$$

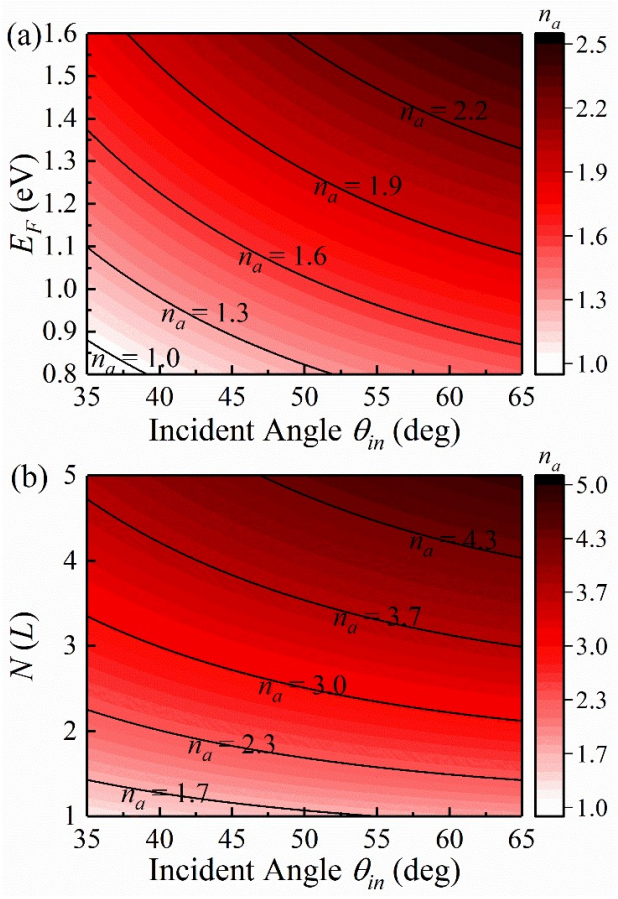

Fig. 2 Estimating analyte refractive index sensing range for (a) E_F is various from 0.8 eV to 1.6 eV when $N=1$, and (b) N is various from 1 to 5 (when $E_F=1.0$ eV at $f=5$ THz). The results are obtained via solving equations (1) and (5).

It can be readily derived from this simplified expression that $k_{spp} \propto n_a^2$, n_s^2 and $k_{spp} \propto \sigma^{-1}$. Thus, the momentum mismatch between the SPP and the light photons can be availably alleviated by increasing the surface conductivity of graphene with high doping levels or with few-layer graphene. Compared with using periodically patterned graphene structures[13, 32] to overcome the mismatch, these methods could avoid the severe deterioration of graphene mobility resulting from the lithography process necessary for fabricating patterned graphene.

The analyte refractive index sensing range are estimated for E_F is various from 0.8 eV to 1.6 eV when $N=1$, and N is various from 1 to 5 (when $E_F=1.0$ eV at $f=5$ THz), as shown in Fig. 2(a) and Fig. 2(b), respectively. The calculations were obtained through solving equations (1) and (5). Obviously, the increase of graphene doping level or graphene layer will make the range of refractive index sensing larger. At the same time, the dynamic modulation of sensing range can be realized according to different graphene doping levels. The maximum measured refractive index of the analyte is up to 5 when N is increase to 5. This indicates that the proposed structure with multilayer graphene can support a very wide refractive index sensing range.

3. Physical Theoretical analysis and simulations of phase properties under SPR

The phase properties of a reflected wave are greatly affected by the excitation of SP, which will show great differences under different excitation situations. The phase of a reflected wave will become a singularity when the minimum of the intensity tends to zero.[33] When a finite width beam of incident radiation is injected on one of the interfaces of the multilayered sensing system (as shown in Fig. 1), the amplitude of reflected wave A_R can be expressed as:

$$A_R = rA_I = |r|e^{i\phi}A_I \tag{6}$$

where r is the amplitude reflection coefficient, A_I is the amplitude of the incident wave and ϕ is the phase shift of the electromagnetic field oscillations of the wave caused by the reflection. It is a smooth function of r (which is relevant to the radiation, the multilayer system, the thickness of sensing layer or the medium's refractive index[34, 35]), which is defined in a complex plane except at the point $r=0$:

$$\begin{aligned}\phi &= \arg r \\ &= \begin{cases} \arctan(\mathrm{Im}r/\mathrm{Re}r) & \text{for } \mathrm{Re}r>0, \\ \arctan(\mathrm{Im}r/\mathrm{Re}r)+\pi & \text{for } \mathrm{Re}r<0 \text{ and } \mathrm{Im}r>0, \\ \arctan(\mathrm{Im}r/\mathrm{Re}r)-\pi & \text{for } \mathrm{Re}r<0 \text{ and } \mathrm{Im}r<0. \end{cases}\end{aligned} \tag{7}$$

The power reflection coefficient (Reflectivity) is

$$R \equiv |r|^2 = rr^* \tag{8}$$

where the symbol * denotes a complex conjugate. Let $r=r(x)$ be a smooth function of an arbitrary real variable x. This variable is relevant to the radiation or the multilayer system (for instance, the incidence angle of the radiation) and the function $R=R(x)$ has a minimum.[34, 35] At the point of the minimum:

$$\left(rr^*\right)' = 0 \tag{9}$$

and

$$\left(rr^*\right)'' > 0 \tag{10}$$

where the symbols ' and " denote first and second derivatives with respect to x. The set of expressions (7) easily yields:

$$\phi' = \mathrm{Im}(r'/r) \tag{11}$$

Furthermore, the function r(x) profile also changes with variations of another variable y (such as the thickness of sensing layer or the medium's refractive index as show in Fig. 1) in such a way that the minimum of R close to zero when y reaches its optimum value.[34, 35] It then follows from formula (9) that $r'/r = -r^{*\prime}/r^*$. Thus, the ratio r'/r at the minimum is always imaginary, that is $\arg(r') - \arg(r) = \pi/2 + n\pi$, where $n=0, \pm1, \pm2,\ldots$, and $r'/r = \pm i|r'|/|r|$. If the second derivative $\left(rr^*\right)'' = r''r^* + rr^{*\prime\prime} + 2|r'|^2$ at the minimum remains greater than a

certain given positive value as the minimum of R approaches zero (i.e., the radius of curvature of the resonant contour does not tend to infinity at the minimum), then it can be inferred that $|r'|$ also remains greater than a certain given positive value. Consequently, combining the above analysis and equation (11), one may conclude that ϕ' at the minimum tends to infinity when the minimum of R approaches zero. Moreover, ϕ' changes its sign as r passes through the point $r=0$ (which corresponds to the case of the variable y goes through its optimum value) due to $r=r(x, y)$ is a smooth function of both x and y in the complex plane. The ratiocination above is entirely relevant to SPR, which possesses a resonant minimum in the dependence of R on incidence angle or radiation frequency. The suppression of the reflectance at the minimum (i.e., R = 0) has been predicted analytically[14] and validated experimentally[19] for Otto prism THz-SPR structures based on attenuated total reflection (ATR) in certain situations. The variable y was the thickness of sensing layer in these previous reports.

2D simulations were built to obtain the reflectance and phase spectra using COMSOL Multiphysics. The unit cell of 2D simulation model is demonstrated in the inset of Fig. 3(a). The periodic boundary conditions applied along the direction of periodicity and the perfectly matched layer (PML) was set to achieve absorbing boundary conditions. The graphene sheet was simulated using Drude permittivity model as mentioned above in the THz regime. This inset also shows the obvious enhancement of the electrical field in the vicinity of graphene surface in resonance. For all following simulations, f is set to 5 THz. Fig. 3 shows the reflectance (a) and phase shift (b) as a function of the incident angle and the absolute gradient of the change in phase between the sample ϕ_{sam} and reference ϕ_{TE} spectrum $\Delta\phi'=\left|d(\phi_{sam}-\phi_{TE})/d(\theta_{in})\right|$ (c) for various thickness of the analyte with MLG at $E_F=1.0$ eV and $n_a=1$. Firstly, it can be see that the reflection spectra exhibit distinct dips resulting from the coupling of energy from the incident wave into the SPP wave. Note that the phase region was extended to display a continuous change. Secondly, the phase spectra exhibit a sharp phase jump that are associated with the interaction between the incident THz wave and SP around the resonant angle. But the reflectance and phase of the TE–polarized wave takes on no resonant features due to no SP modes can be excited in this geometry. Therefore, it is calculated as a reference. Moreover, the steepness of phase jump increases dramatically as the analyte thickness t_a increases to its optimum (i.e., R = 0). However, it will reduce gradually and the sign of the slope is opposite (which is consistent with the theoretical analysis above) with a further increase of t_a. At the same time, the phase spectra vary in shape that it is not monotonous but possesses a maximum and a minimum near the resonant angle. Namely, the profile of phase jump change from step-like contour to Fano lineshape when the system passes through the optimum SPR conditions. Importantly, graphene has strong adsorption to biomolecules because of π-stacking interactions and the high surface to volume ratio.[36] It will give rise to the increase of thickness of molecule layer adsorbed on graphene surface

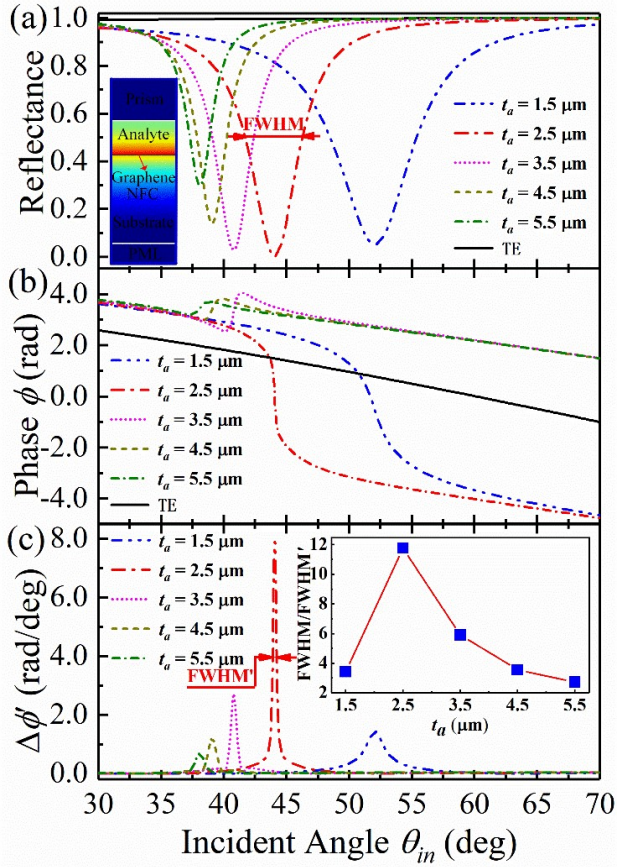

Fig. 3 Reflectance (a) and Phase shift (b) as a function of the incident angle for various thickness of the analyte and TM polarization with MLG at $f=5$ THz , $E_F=1.0$ eV and $n_a=1$. The phase of TE polarization is shown for comparison. The inset shows the unit cell of 2D simulation model and the electric field distributions. The absolute gradient of the change in phase between the sample and reference spectrum, *i.e.*, $\Delta\phi'$, $\Delta\phi'=\left|d(\phi_{sam}-\phi_{TE})/d(\theta_{in})\right|$ (c). The inset shows the ratio of FWHM of reflection spectra and FWHM' of $\Delta\phi'$ spectra.

when a (bio)chemical sensing is carried out. As a result, the optimum SPR conditions will change. Thus, it may be provide for ultrahigh sensitivity to (bio)chemical sensing by monitoring the inversion of phase jump. Remarkably, the region of the phase jump just take place around the point of R minimum. From the Fig. 3(c), it can be further seen clearly that all $\Delta\phi'$ show a sharp peaks which are narrower than the reflectance dips as shown in Fig. 3(a). As can be seen in the inset of Fig. 3(c), the maximum ratio of FWHM of reflection spectra and FWHM' of $\Delta\phi'$ is up to 12 at the optimum resonant angle where $R=0$, which making phase change potentially a very effective indicator for the detection of small refractive index changes in the mediums. Note that the variation of the width of $\Delta\phi'$ is different from reflection spectra (which its width broadened by radiative damping of SPP that couple back to the prism) as shown in Fig. 3(a). The reason is that the steepness is irrelevant to the width of R contour, but defined by a parameter (such as analyte thickness) that reduces the minimum down to zero.[33]

4. Sensing performance based on phase detection

Fig. 4 plots the phase spectra (a) and absolute gradient of phase change spectra (b) for various Fermi level energy from 0.8 to 1.6 eV with MLG at $n_a = 1$. As can be seen, there is a significant left–shift in the phase jump as the Fermi level energy of graphene increases due to the fact that the SPP wavenumber reduces with increasing E_F at a given frequency as shown in equation (5). So the resonant angle of SPR can be dynamically tuned via adjusting graphene E_F. Of particular interest is the phase spectrum following a Fano lineshape at the case of $E_F = 0.8$ eV, which is different from other phase spectra. The reason for this is that the minimum value of its reflectance can't passes through zero via changing the analyte thickness. Thus, it only exhibits a profile of Fano lineshape at optimal resonance conditions. Furthermore, it can be seen clearly that the absolute gradient of phase change spectra exhibit a sharp peaks. Correspondingly, the detection accuracy (DA, which is defined as the reciprocal of FWHM', *i.e.*, $\mathrm{DA} = 1/\mathrm{FWHM}'$) increases from 0.93 deg-1 for $E_F = 0.8$ eV to 3.70 deg-1 for $E_F = 1.6$ eV as shown in the inset of Fig. 4(b). Therefore, the DA of sensing systems can be promoted by increasing graphene E_F suitably. Similar trends in the shift of phase jump and sharp peaks are observed in the phase spectra of Fig. 5(a) and absolute gradient of phase change spectra of Fig. 5(b) for various number of graphene layer N from 1 to 5 at $E_F = 1.0$ eV and $n_a = 1$, respectively. The pronounced left–shift in the phase jump occur with the increases of N for the SPP wavenumber reduces. It can be found that multilayer graphene based sensing structures also possess a high DA as shown in the inset of Fig. 5(b). The maximum DA is up to 4 deg-1 for $N = 5$.

In order to have a further insight into the performance of reflective index sensing based on phase detection. The resonant

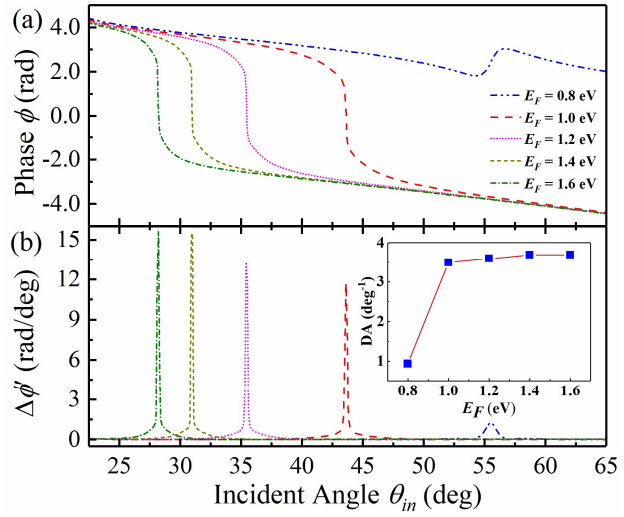

Fig. 4 Phase spectra (a) and absolute gradient of phase change spectra (b) for various Fermi level energy (E_F) from 0.8 to 1.6 eV with MLG at $f = 5$ THz and $n_a = 1$. The inset shows the variation of DA (which is defined as the reciprocal of FWHM', *i.e.*, $\mathrm{DA} = 1/\mathrm{FWHM}'$) with different E_F. For all cases, the thickness of analyte t_a was varied between 2.2–5.5μm.

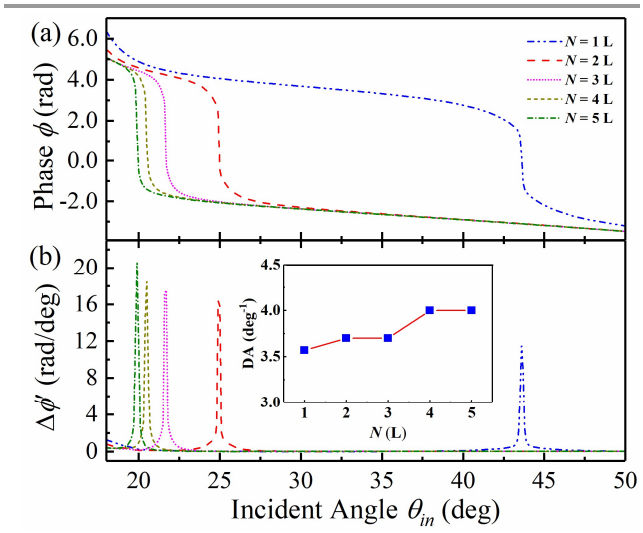

Fig. 5 Phase spectra (a) and absolute gradient of phase change spectra (b) for various No. of graphene layer N from 1 to 5 at $f = 5$ THz, $E_F = 1.0$ eV and $n_a = 1$. The inset shows the variation of DA with different N. For all cases, the thickness of analyte t_a was varied between 2.6–8.5μm.

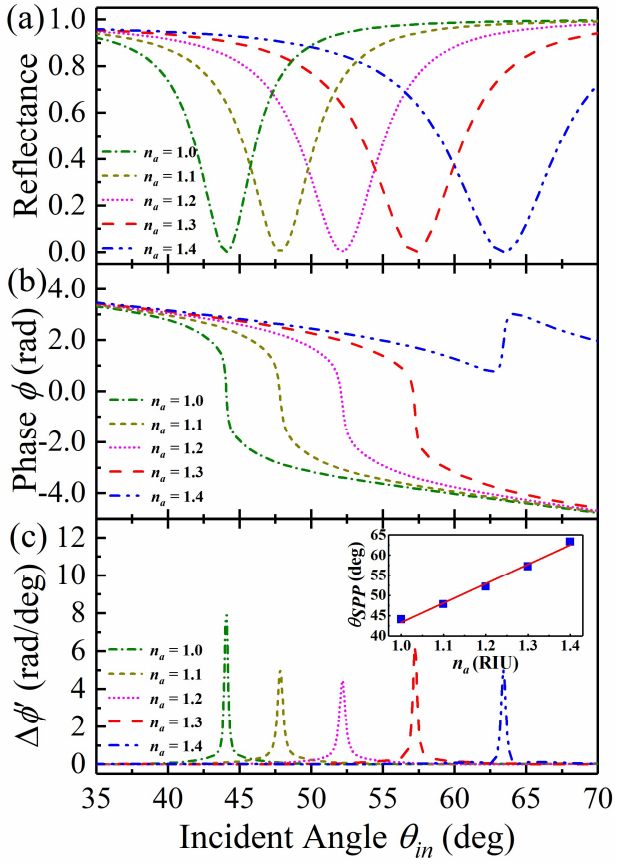

Fig. 6 Reflection spectra (a), Phase spectra (b) and absolute gradient of phase change spectra (c) for various reflective index of the analyte n_a with MLG at $f = 5$ THz, $E_F = 1.0$ eV and $t_a = 2.5$ μm. The inset shows the linear fitting of the scatter data of n_a and its corresponding optimal resonance angle ϑ_{SPP}.

spectra for various reflective index of the analyte n_a from 1.0 to 1.4 with MLG at $E_F = 1.0$ eV and $t_a = 2.5$ μm are plotted in the Fig. 6. As can be seen, the resonant spectra right shift with the increases of n_a for the SPP wavenumber increases (easily seen from expression (5)). Compared Fig. 6(a) with Fig. 6(c), it is obviously observed that the FWHM′ of $\Delta\phi'$ spectra are much less than the FWHM of reflection spectra. The optimal resonance angle ϑ_{SPP} are plotted against their respective refractive indexes in the inset of Fig. 6(c). The red solid line is a linear fit given by $\theta_{SPP} = 47.96 n_a - 4.62$. This gives a sensitivity (defined as the change in ϑ_{SPP} per RIU) of 47.96 deg/RIU. Hence using phase jumps as our SPR sensor readout response, the FOM values for n_a from 1.0 to 1.4 are 171, 94, 94, 145, and 126, respectively. These values are much higher than the FOM values of 11, 9, 8, 7 and 6 calculated based on reflection spectra and previously reported values.[37, 38]

The resonant spectra for various the imaginary part of complex reflective index ($\tilde{n} = n + i\kappa$) in the analyte κ_a from 0.02 to 0.10 with MLG at $E_F = 1.0$ eV , $t_a = 2.5$ μm and $n_a = 1$ are also plotted in the Fig. 7. From the Fig. 7(a), it can be seen clearly that the FWHM of reflection spectra is broadened by the increase of the damping of SP due to the increase of κ_a, but the angular position of the resonance dip remains approximately constant. The reflectance at optimum resonant angle R_{SPP} increases from 0.04 for $\kappa_a = 0.02$ to 0.34 for $\kappa_a = 0.10$. As a result, the steepness of phase jump reduces dramatically with the increase of κ_a as shown in Fig. 7(b). From the Fig. 7(c), it also can be observed that the absolute gradient of phase change at optimum resonant angle $\Delta\phi'_{SPP}$ reduces from 1.31 rad/deg for $\kappa_a = 0.02$ to 0.15 rad/deg for $\kappa_a = 0.10$. The R_{SPP} and $\Delta\phi'_{SPP}$ are plotted against their respective imaginary part of refractive indexes in the inset of Fig. 7(c). Also, curve fitting were performed for these scatter data to compare the sensitivities of this two detection methods. From the slope of these two curves, it is clearly to see that the characteristic phase jumps on our SPR structure, as a readout response to carry out the imaginary part of refractive index sensing that also outperforms amplitude based measurements, which may be applied for ultrasensitive viruses or microorganism detection in THz regime.[39]

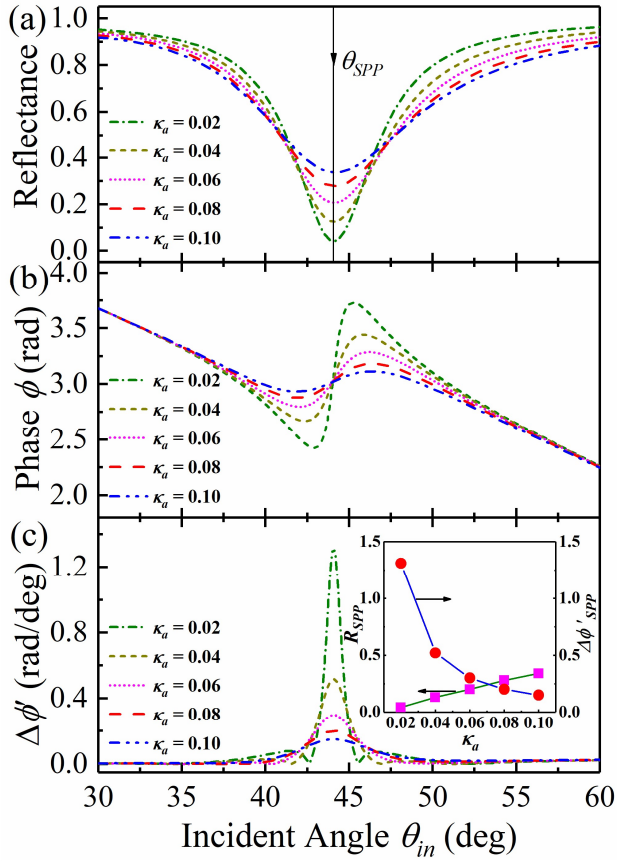

Fig. 7 Reflection spectra (a) , Phase spectra (b) and absolute gradient of phase change spectra (c) for various the imaginary part of reflective index in the analyte κ_a with MLG at $f = 5$ THz , $E_F = 1.0$ eV , $t_a = 2.5$ μm and $n_a = 1$. The inset shows fitting curves of the scatter data of κ_a and its corresponding reflectance (R_{SPP}) and absolute gradient of phase change $\Delta\phi'_{SPP}$ at optimal resonance angle ϑ_{SPP}.

5. Conclusions

In this work, we make full use of the adjustable properties of graphene plasmon to propose a graphene/insulator stack (GIS) based tunable terahertz (THz) plasmonics sensor. We draw attention to an oft-neglected source of information in THz–SPR sensing study that the phase of the electromagnetic fields. The comprehensive description of THz–SPR phase properties has been accomplished by theoretical analysis and a number of numerical simulations. The results showed that a small change in the refractive index of the medium will result in a sharp change in phase of the reflected wave, whereas the intensity changes little against the background of the resonance reflection minimum, which making phase change potentially a very effective indicator for the detection of small refractive index changes in the mediums. A FOM as high as 171 was achieved based on terahertz phase detection, which is about 16 times of the FOM obtained via traditional terahertz amplitude based measurement method, making refractive index sensing possible on analyte with higher loss. The prominent characteristics of this new method would pave the way for conducting high–performance THz–SPR sensing.

Acknowledgements

We gratefully acknowledge support from the National Natural Science Foundation of China (51675103), the State Key Laboratory of Mechanical System and Vibration (MSV-2018-07), and the Shanghai Natural Science Fund (18ZR1414200).

References

1 P. H. Siegel, *IEEE Trans. Microwave Theory*, 2002, **50**, 910.
2 J. F. Federici, B. Schulkin, F. Huang, D. Gary, R. Barat, F. Oliveira and D. Zimdars, *Semicond Sci. Technol*, 2005, **20**, S266.
3 M. Walther, P. Plochocka and B. Fischer, *Biopolymers*, 2002, 67, 310.
4 W. Xu, L. Xie and Y. Ying, *Nanoscale*, 2017, **9**, 13864.
5 P. H. Siegel, *IEEE Trans. Microwave Theory*, 2004, **52**, 2438.
6 A. G. Markelz, A. Roitberg and E. J. Heilweil, *Chem. Phys. Lett.*, 2000, **320**, 42.

7 C. R. Williams, M. Misra, S. R. Andrews and S. A. Maier, *Appl. Phys. Lett.*, 2010, **96**, 97.
8 J. B. Pendry, L. Martin-Moreno and F. J. Garcia-Vidal, *Sci.*, 2004, 305, 847.
9 C. R. Williams, S. R. Andrews, S. A. Maier, A. I. Fernández-Domínguez, L. Martín-Moreno and F. J. García-Vidal, *Nat. Photonics*, 2008, **2**, 175.
10 F. J. Garciavidal, L. Martínmoreno, J. B. Pendry, *J. Opt. A-Pure Appl. Opt.*, 2005, **7**, S97.
11 A. P. Hibbins, B. R. Evans and J. R. Sambles, *Sci.*, 2005, **308**, 670.
12 Y. Zhao and Y. Zhu, *Nanoscale*, 2015, **7**, 14561.
13 L. Ju, B. Geng, J. Horng, C. Girit, M. Martin, Z. Hao, H. A. Bechtel, X. Liang, A. Zettl, Y. R. Shen and F. Wang, *Nat. Nanotechnol.,* 2011, **6**, 630.
14 C. H. Gan, Appl. *Phys. Lett.*, 2012, **101**, 111609.
15 K. F. Mak, M. Y. Sfeir, Y. Wu, C. H. Lui, J. A. Misewich and T. F. Heinz, *Phys. Rev. Lett.* 2008, **101**, 196405.
16 C. F. Chen, C. H. Park, B. W. Boudouris, J. Horng, B. Geng, C. Girit, A. Zettl, M. F. Crommie, R. A. Segalman and S. G. Louie, *Nat.*, 2011, **471**, 617.
17 A. Purkayastha, T. Srivastava and R. Jha, *Sens. Actuators. B: Chem.*, 2016, **227**, 291.
18 Y. Huang, S. Zhong, H. Yao and D. Cui, *IEEE Photonics J.*, 2017, **9**, 1.
19 B. Ng, J. Wu, S. M. Hanham, N. Klein, Y. Liew, M. Breese, M. Hong and S. Maier. *Advan. Opt. Mater.*, 2013, **1**, 543.
20 T. Holmgaard and S. I. Bozhevolnyi, *Phys. Rev. B–Condensed Matter.*, 2007, **75**, 245405.
21 J. M. Siqueiros, R. Machorro and L. E. Regalado, *Appl. Opt.*, 1988, **27**, 2549.
22 D. B. Farmer, H. Y. Chiu, Y. M. Lin, K. A. Jenkins, F. Xia and P. Avouris, *Nano Lett.*, 2009, **9**, 4474.
23 D. R. Smith, E. V. Loewenstein and R. L. Morgan, *Appl. Opt.*, 1973, **12**, 398.
24 L. A. Falkovsky and A. A. Varlamov, *Eur. Phys. J. B–Condensed Matter.*, 2006, **56**, 281.
25 D. K. Efetov and P. Kim, *Phys. Rev. Lett.*, 2010, **105**, 256805.
26 G. W. Hanson, *J. Appl. Phys.*, 2008, **103**, 064302.
27 M. Jablan, H. Buljan and M. Soljačić, *Phys. Rev. B.*, 2009, **80**, 245435.
28 A. Vakil and N. Engheta, *Sci.*, 2011, **332**, 1291.
29 H. Yan, X. Li and B. Chandra, *Nat. Nanotechnol.*, 2012, **7**, 330.
30 J. Horng, C. F. Chen, B. Geng, *Phys. Rev. B–Condensed Matter*, 2011, **83**, 165113.
31 C. H. Gan, H. S. Chu and E. P. Li, *Phys. Rev. B–Condensed Matter.*, 2012, **85**, 117.
32 W. Tang, L. Wang, X. Chen, C. Liu, A. Yu and W. Lu, *Nanoscale*, 2016, **8**, 15196.
33 P. I. Nikitin, A. A. Beloglazov, V. E. Kochergin, M. V. Valeiko and T. I. Ksenevich, *Sens. Actuators B Chem.*,1999, **54**, 43.
34 E. Fontana, R. H. Pantell and M. Moslehi, *Appl. Opt.*, 1988, **27**, 3334.
35 J. R. Sambles, G. W. Bradbery and F. Yang, *Contemp. Phys.*, 1991, **32**, 173.
36 P. K. Maharana and R. Jha, *Sens. Actuators B Chem.*, 2012, **169**, 161.
37 L. Cong, S. Tan, R. Yahiaoui, F. Yan, W. Zhang and R. Singh, *Appl. Phys. Lett.*, 2015, **106**, 031107.
38 Y. Zhang, T. Li, B. Zeng, H. Zhang, H. Lv, X. Huang, W. Zhang and A. K. Azad, *Nanoscale*, 2015, **7**, 12682.
39 D. K. Lee, J. H. Kang, J. Kwon, J. S. Lee, S. Lee, D. H. Woo, J. H. Kim, C. S. Song, Q. H. Park and M. Seo, *Sci. Rep*, 2017, **7**, 8146.